RSC Advances

Performance and polarization studies of the magnesium-antimony liquid metal battery with the use of *in-situ* reference electrode

P.K. Leung[1] [*], S.C. Heck[2], T. Amietszajew[1], R.J. Dashwood[1], R. Bhagat[1]

1) WMG, University of Warwick, Coventry, United Kingdom, CV4 7AL.

2) Department of Materials Engineering, University of São Paulo, São Carlos, Brazil, 13563-120.

*Corresponding author: P.leung@uma.es

Abstract

This work presents the performance and polarization studies of a magnesium-antimony liquid metal battery with the use of *in-situ* pseudo reference electrode at high operating temperature (*c.a.* 700 $^{\circ}$C). Due to the immiscibility of the contiguous salt and metal phases, the battery appears as three distinct layers: (1) positive electrode, (2) electrolyte and (3) negative electrode layers. The configuration of the *in-situ* reference electrode within the three floating liquid layers is described and is to avoid direct electrical contact/ short circuit with the other electrodes. Electrochemical tests, including linear sweep voltammetry, impedance spectroscopy and galvanostatic cycling, evaluate the performance of a magnesium-antimony battery under a range of operating temperatures and current densities. Through the polarization studies, the area resistance of the negative, positive electrodes and the overall battery are found to be *c.a.* 0.55, 0.65 and 1.20 Ω cm^{-2}, respectively. In a typical 1 h charge/discharge per cycle experiment, average round-trip energy efficiencies of *c.a.* 64 % are obtained at 60 mA cm^{-2} with a slight deterioration after subsequent cycles. In these tests, the half-cell measurements also indicate that the sprayed layer of boron nitride at the reference electrode is chemically stable and shown to be an effective electrical insulator for prolonged operation at high temperature (*c.a.* 700 $^{\circ}$C).

Keywords: Liquid-metal battery, Magnesium-antimony, Molten-salts, Polarizations, Reference electrode.

1) Introduction

Due to the increasing demand of renewable energy sources, recent efforts have focused on the development of low-cost, efficient and safe energy storage systems for grid-scale and load-levelling applications [1-2]. Among different types of energy storage technologies, increasing attention has been given to the development of aqueous rechargeable batteries [3-6] and molten salt batteries [7-9] attributed to their attractive power output and safety properties.

In spite of these merits, these systems, such as redox flow batteries (RFBs) [5-6] and sodium metal chloride (NaMCl) batteries [7-8] often require high-cost materials as the active materials or the necessary components. To address this issue and promote the widespread use of renewable energy sources, molten-salt liquid metal batteries based on earth-abundant and low-cost metals have been introduced by Massachusetts Institute of Technology (USA) [10-16] in 2012. The proposed system uses low-cost molten salt electrolyte instead of ceramic electrolyte (sodium-conducting beta-alumina electrolyte) as in conventional sodium-based molten salt batteries [7-8]. The resulting system comprises of three liquid metal layers as the anode, electrolyte and cathode materials. These layers float on the top of one another due to the density differences and immiscibility. The liquid nature enables a significant decrease in assembly cost and facilitates the scale-up process [17-20].

By taking account of the chemical and physical properties of different liquid metal couples, including electrode potential, specific density, melting temperature and alloy compatibility, several liquid metal chemistries — (1) magnesium-antimony, (2) calcium-bismuth and (3) sodium-mercury, have been proposed in the past few years. Despite the proof of concept, the information of the charge-discharge cycling and polarization performances of these systems remains very limited in the literatures. Among the proposed chemistries, magnesium-

antimony battery uses some of the lowest cost metals as the active materials (Mg $ 5 Kg^{-1}, Sb

$ 7 Kg^{-1}[12]) and has received significant industrial investments (i.e. Ambri Inc., USA) for

near-term commercialization [13].

In a fashion similar to most rechargeable batteries, electrons are transferred between the two

electrodes through an external circuit during the charge and discharge processes. In a molten

salt electrolyte, energy is released by forming a liquid metal magnesium-antimony alloy at

the positive electrode, while the reversible reactions enable the energy to be stored by

reducing the deposited metal in the alloy back to magnesium ions (Mg(II)) during the

charging process. Schematics of the charge and discharge processes of the magnesium-

antimony battery are illustrated in Figure 1, in which the half- and overall cell reactions are

represented as follows:

$$\text{Negative electrode:} \qquad Mg \leftrightarrow Mg^{2+} + 2\ e^- \qquad\qquad (1)$$

$$\text{Positive electrode:} \qquad Mg^{2+} + 2\ e^- \leftrightarrow Mg\ (\text{in Sb}) \qquad\qquad (2)$$

$$\text{The overall cell reaction:} \qquad Mg \leftrightarrow Mg\ (\text{in Sb}) \qquad\qquad (3)$$

The discharge capacity of the magnesium-antimony battery depends on the magnesium

content in the antimony alloy during the discharge process. This can be rationalized by using

a binary phase diagram to indicate the alloy composition range at different temperatures. To

avoid the formation of the solid phase Mg_3Sb_2 [21], the maximum weight percentage of

magnesium is about 8.7 % as illustrated in Figure 2 at the operating temperature of 700 ^{o}C.

This gives a theoretical capacity of *c.a.* 1600 mA h when 0.74 and 8.5 grams of magnesium

and antimony are used, respectively, as an Mg-Sb alloy. By mixing the selected halide salts

(KCl, NaCl and $MgCl_2$) at certain molecular ratio, the melting temperatures can be as low as

383 ^{o}C estimated by the FactSage$^®$ software (Figure 3), which is significantly lower than the

melting temperature of each individual salt ($T_{m.t. \; NaCl}$ = 801 ^{o}C, $T_{m.t. \; KCl}$ = 771 ^{o}C and $T_{m.t. \; NaCl}$ = 714 ^{o}C) and the operating temperature (700 ^{o}C) of the resulting battery.

In addition to this, the open circuit potential of the liquid-metal battery is dependent on the amounts of pure magnesium and that dissolved in the antimony alloy as described in the theoretical expression of Nernst equation:

$$E_{cell} = RT / 2 \; F \; (\ln \; [\alpha_{Mg(in \; Sb)} / \; \alpha_{Mg} \;]) \qquad (4)$$

where R is the real gas constant (8.31 J K^{-1} mol^{-1}), T is the absolute temperature, F is the Faraday's constant (equals 96, 485 C mol^{-1}), α_{Mg} and $\alpha_{Mg(in \; Sb)}$ are the activities of pure magnesium and that dissolved in the antimony alloy, respectively. In order to improve the understanding of the liquid-metal battery, this work further investigated the cycling performance and the half-cell polarizations of a laboratory scale cell with the utilization of an *in-situ* reference electrode. The reference electrode used in liquid liquid batteries needs to be chemically stable at high temperature (*c.a.* 700 ^{o}C) and to avoid direct electrical contact / short circuit with the other electrodes within the structure of the three floating liquid layers.

This unique circumstance makes it challenging to incorporate a reference electrode in a small-scale laboratory cell (< 20 mm diameter), thus explaining the very limited information of this type of battery regarding their half-cell performances. By proposing a simple configuration of the three-electrode set-up, measurements of polarizations and half-cell electrode potentials can be made available in the charge-discharge cycles. In this work, a tungsten wire was used as a pseudo-reference electrode and was spray-coated by an insulating layer of boron nitride with its tip exposed in the middle of the electrolyte layer. With the insertion of a reference electrode, experimental results show that the magnesium-antimony liquid metal battery was capable of charge-discharge cycling at high energy efficiencies (> 60 %) under a range of current densities (15 – 80 mA cm^{-2}). In this range, the

area resistance of the negative and positive electrodes were *c.a.* 0.55 and 0.65 Ω cm^{-2}, respectively. By cycling the battery at 60 mA cm^{-2} for 1 h, 8 cycles were obtained with the average voltage and energy efficiencies of *c.a.* 64.5 and 64.0 %, respectively.

2) Experimentals

2.1) Liquidus projection simulation

Ternary liquidus projection and eutectic compositions of molten salt systems of different compositions and temperatures were calculated from thermodynamic data sing a FactSage$^{®}$ software (GTT Technologies GmbH), which is based on the Calculation of Phase Diagram and Thermodynamics (CALPHAD) method [22].

2.2) Battery charge-discharge experiments

Electrode materials were analytical grade metallic magnesium and antimony metals of 99.5 % purity provided by Alfa Aesar Inc., UK. The salt electrolyte was based on a mixture of anhydrous potassium chloride, sodium chloride and magnesium chloride salts (ACROS Inc., UK, at 99 %) at molecular ratio of 20: 30: 50 [12]. These materials were contained in a gold-plated glassy carbon crucible (16 mm inner diameter with boron nitrite coating, HTW, Germany), in which boron nitrite (Ekamold TG, ESK GmbH, Germany) was spray-coated on its wall to avoid direct electrical contact between the two electrode layers.

During the assembly of the battery, a single cell was prepared at the partially charged state (at *c.a.* 66.6 % state-of-charge (SOC)) by initially adding 8.5 grams of antimony and small

amount of the magnesium (0.25 grams) to the bottom of the crucible as the positive electrode layer.

Following this, 8 grams of the halide salt electrolyte was added on the top of the antimony layer as the middle layer. On the top of these two layers, magnesium granules (1.5 grams) were further added to form the negative electrode layer, which was electrically connected by a graphite rod (9 mm diameter) serving as the current lead. On the other hand, the stainless steel platform underneath the crucible serves as a mechanical support and a current collector for the positive electrode.

As shown in Figure 4, the crucible was mechanically supported by the stainless steel rod and was placed inside the quartz tube (380 mm length). The quartz tube was then sealed by ceramic papers (Product 299-3689, RS UK) and carbon o-rings (SLN 200, Klinger, UK), and subsequently loaded into a vertical tube furnace. During the preparation and testings, high purity argon gas (99.99 %) was purged into the tube continuously at > 0.2 cm^3 s^{-1} to avoid the oxidation and burning of the cell components at high temperatures. The temperature of the battery was controlled and measured by an electronic thermocouple, which was attached on the surface of the carbon crucible. In order to prepare a dry and homogeneous molten salt electrolyte, the quartz tube was heated to 180 ^{o}C and maintained at this temperature for over 24 h. Since then, the battery was heated to 700 ^{o}C at a rate of 3 ^{o}C min^{-1}. The meltdown of the active metal and halide salt eventually led to the formation of the three liquid layer structure, the open-circuit cell voltage became available and rose up to *c.a.* 0.46 V. In certain experimental set-ups, as shown in Figure 5, the energy-dispersive X-ray spectroscopy (EDS) has confirmed that the negative and positive electrode layers were based on pure magnesium (100 w.t. % magnesium) and antimony-magnesium alloy (3.2 w.t. % magnesium, 96.8 % w.t. % antimony). This is possibly due to the fact that any formation of magnesium alloy with

antimony sinks to the bottom as the volumetric mass density is much higher than the chloride melt layer.

After the significant volume change in the melting process, the reference electrode was then inserted down to the middle of the electrolyte until an independent electrode potential different from the cell voltage was obtained. The reference electrode was a thin tungsten wire of 1.5 mm diameter (99.95 %, Good fellow Inc., UK) with its tip exposed to the electrolyte layer, while the rests of the wire was electrically insulated by a thick layer of boron nitride (c.a. 60 – 90 micron). Prior to the experiments, the electrode potential of the tungsten wire has been confirmed to be stable in the chloride melt for over 4 days by comparing its relevant potential with a new tungsten wire. As shown in Figure 6, the optical and scanning electron micrograph images of the boron nitrite layers were very similar before and after immersion in the chloride melt. The use of tungsten as a pseudo-reference electrode has also been evaluated by the work of Misra *et al.* [23] in chloride melts at similar operating temperature (650 ^{o}C), in which tungsten was reported to have superior chemical stability over stable metals, such as platinum, molybdenum, hafnium, tantalum and stainless steel.

Unless otherwise stated, the operating temperature was set at 700 ^{o}C. The active areas were *c.a.* 1.2 cm^2 with respect to the average area of the negative and positive electrodes. Since the battery was prepared at partially charged state (*c.a.* 66.6 % SOC), the battery needed to be firstly discharged down to 0.2 V at 60 mA cm^{-2} (72 mA). The duration of the discharge process was typically more than 14 hours, leading to a discharge capacity of > 1000 mA h, which is slightly lower than the theoretical value (*c.a.* 1050 mA h for *c.a.* 66.6 % SOC) estimated by the Faraday's law.

During the charge-discharge cycling, the magnesium-antimony battery was charged at constant current density of 60 mA cm^{-2} (72 mA) for 1 h and then discharged for the same

period of time at the same current density (60 mA cm^{-2}) using a Bio-logic VMP3 potentiostat (Bio-logic SAS, France).

Voltage and energy efficiencies of the liquid metal batteries were obtained from the following formulae:

$$\text{Voltage efficiency} = V_d / V_c \times 100 \text{ \%} \tag{5}$$

$$\text{Energy efficiency} = j_d V_d \Delta t_d / j_c V_c \Delta t_c \times 100 \text{ \%} \tag{6}$$

where V is the cell voltage and j is the applied current density, c and d denote the charge and discharge processes, respectively.

2.3. Linear sweep voltammetry

Based on the experimental set-up of the charge-discharge cycling experiment, linear sweep voltammetry was carried out in a partially charged (*c.a.* 66.6 % SOC) liquid metal battery with the aforementioned reference electrode and potentiostat. The operating conditions, including temperature and electrolyte compositions, were the same as that described in Section 2.1. By using linear sweep voltammetry, the cell voltage *vs.* current density response was obtained by sweeping the cell voltage linearly from –0.5 to +1.5 V at a scan rate of 20 mV s^{-1}. To measure the electrode potential response, the potential of each electrode was measured independently using the other electrode as the counter electrode. All electrode potential measurements were made against the tungsten pseudo-reference electrode.

2.4. Electrochemical impedance spectroscopy

Electrochemical impedance spectroscopy was carried out in a partially charged (*c.a.* 66.6 % SOC) liquid metal battery using a VMP potentiostat between 550 and 700 ^{o}C. The measurements were obtained in a potentiostatic mode with an applied voltage amplitude of 10 mV at the open circuit voltages (–1.2 to +0.5 V). The frequency range was between 100 kHz and 1 mHz, which took up to 15 minutes to finish each measurement. By using the EC-Lab Electrochemistry software, the full impedance spectrum was presented and analysed in a Nyquist plot, in which a vertical line and a depressed semi-circle were observed. The electrochemical data was then extracted by fitting into a relevant R $L(Q$ (RW)) equivalent circuit model, where R is a resistor, L is an inductor, Q is a constant phase element and W is a Warburg diffusion element.

3. Results and discussions

3.1. Operating temperatures

According to the experimental procedures described in Section 2.1., the assembled magnesium-antimony battery was prepared at a partially charged state (*c.a.* 66.6 % SOC) and heated gradually to 700 ^{o}C. The heating process underwent the meltdown of the salts (*c.a.* 400 ^{o}C) and the active materials (*c.a.* 630 – 650 ^{o}C), leading to the formation of the three liquid layer structure. Once the three liquid layer structure was formed, the system could function as a battery and exhibit a relatively high open-circuit voltage (> 0.4 V). Figure 7 shows the responses of the open-circuit cell voltage under a gradual increase in temperature between 500 and 765 ^{o}C.

When the temperature was lower than 525 $^{\circ}$C, no cell voltage was obtained due to the absence of the molten salt electrolyte. Once the halide salts melted and formed the electrolyte layer, the cell voltage became available but observed with fluctuations. With the further increase of temperature, the open-circuit cell voltage initially dropped towards –1.04 V. This is attributed to the partial mixings of the solid metals of magnesium and antimony with the electrolyte layer. In the presence of the molten salt electrolyte, the potential difference between the unmixed magnesium and antimony can be up to ± 2.0 V by taking the references that the standard electrode potentials of these two metals in aqueous (non-molten salt) electrolytes are – 2.4 V vs. SHE and – 0.4 V vs. SHE, respectively. However, the partial mixing of these metal solid may result in much smaller potential differences than the case of the unmixed condition.

When the temperature continued to increase to higher than 625 $^{\circ}$C, the active metals of both magnesium and antimony began to melt, as the theoretical melting temperatures of these metals are 625 and 630 $^{\circ}$C, respectively. The melting of these metals enables magnesium to float on the top over the other layers attributed to its low specific density (1.738 g cm^{-3}). The formation of the three metal layers led to a drastic increase in cell voltage towards *c.a.* 0.46 V at a temperature range between 690 and 710 $^{\circ}$C. The corresponding magnesium and antimony electrode potentials were – 0.47 and – 0.10 V *vs.* W, respectively. However, further increase in temperature over 710 $^{\circ}$C was observed to decrease the overall cell voltage down to 0.23 V.

In addition to phase change and electrode potential, temperature has high influence on electrode kinetics, diffusion dynamic and internal resistance. To evaluate these issues, impedance spectroscopy has been used in different battery systems, including previous magnesium-antimony liquid metal batteries [12, 24]. Figure 8 shows the Nyquist plot of the liquid metal battery at different temperatures (550 – 700 $^{\circ}$C) over the range between 100 kHz

and 1 mHz. In liquid metal battery, the vertical line at the intercept represents the ohmic resistance (R_Ω) and the inductive components (L) within the electrical circuit, while the pseudo-capacitive characteristic of the depressed semi-circle acted as an imperfect capacitor (CPE or Q) and represented the double layer behaviour. The diffusion or concentration change of the metal ions in the liquid electrolyte medium is often indicated by a straight line inclined at 45° (W) at lower frequencies (< 1 Hz) in the complex impedance plane.

At elevated temperatures, the impedance spectra tended to shift towards smaller values along the real impedance axis. These spectra can be further fitted into the R_Ω L (Q ($R_{c.t.}W$)) equivalent circuit model (Randles (1947) equivalent circuit) as used in the reported calcium-bismuth liquid metal battery [12]. Such equivalent circuit takes account of the several features of most battery systems: electrode chemical reactions, formation of double layers, adsorption and diffusion contributed to the particle surface impedance [24]. The high frequency intercept is the ohmic resistance (R_Ω), representing the overall electrical resistance of the battery, including the series resistance of the electrodes, electrolyte, connector terminals and wires; L is the inductance of the outer lead; Q is the constant phase element representing the area/ capacity of the electrodes; the lower frequency $R_{c.t.}$ is the charge-transfer resistance representing the reaction kinetics at the electrode-electrolyte interface; and σ is the generalised Warburg impedance coefficient through the electrodes.

The model fitting results are summarized in Table 1, which shows that the ohmic resistance decreased gradually at increased temperatures from 550 to 700 $^\circ$C . This can be due to the increase in ionic conductivity of the halide salt electrolyte (KCl-NaCl-MgCl$_2$) [12, 13]. Since the ionic conductivity is high in molten salt electrolyte, the overall ohmic resistance was relatively small. At the operating temperature of 700 $^\circ$C, the overall ohmic resistance was 1.2 Ω cm^2, comparable to that (0.98 – 1.21 Ω cm^2) obtained by Sadoway *et al.*[12] in their

magnesium-antimony batteries. The difference in ohmic resistance can be due to the Rayleigh-Taylor instability of a smaller cell and the thicker electrolyte layer used to accommodate the additional reference electrode.

Assuming the fact that constant phase element, Q, is influenced by the overall area/ capacity of the electrodes, this value is expected to remain similar unless significant structural change/ damage take place in such temperature range. In general, elevated temperature tends to facilitate the electrode charge-transfer kinetics and the ionic diffusion process as indicated by the decreases in the charge transfer resistance value, $R_{c.t.}$, and the Warburg impedance coefficient, σ. Compared to the ceramic separators used in conventional molten salt batteries, the liquid-liquid electrolyte interface of the liquid metal battery enables faster electrode kinetics. Furthermore, the liquid-state diffusion is far more efficient than the ceramic separator in terms of mass transports of both reactants and products [12, 13, 15].

3.2. Current densities

The influences of current density on the electrode potentials and the cell voltage of a partially charged magnesium-antimony liquid metal battery were evaluated initially by linear sweep voltammetry. The operating conditions, including temperature and electrolyte compositions, were the same as those described in section 3.1.

By considering the open circuit voltage was *c.a.* 0.46 V, the cell voltage was swept at a relatively wide potential range between – 0.5 and + 1.5 V at 20 mV s^{-1}. As shown in Figure 9, the linear relationships between the electrode potentials and the current density indicate that the mass transport of active materials is not limited even at high current densities of over 1000 mA cm^{-2} in both charge and discharge processes. When the current density was

increased by 500 mA cm^{-2}, the voltage drop in the discharge process was *c.a.* 500 mV, leading to an overall ohmic resistance of *c.a.* 1.00 Ω cm^2. This value was comparable to the ohmic resistance value (*c.a.* 1.20 Ω cm^2) obtained in Section 3.1. using impedance spectroscopy, in which the measurement is based on the response of the battery to a small applied perturbation (i.e. AC signal) at the open circuit potential over a pre-determined frequency range.

In the linear sweep voltammetry, the responses of the half-cell electrode potentials were recorded and represented in Figure 9. Similar to the cell voltage, the relationships of the two electrode potentials were linear with current densities but with smaller gradients. This is because the cell voltage is composed of the half-cell electrode potentials as expressed in equation (7):

$$E_{cell} = E_{pos} - E_{neg} \tag{7}$$

in which E_{pos} and E_{neg} are the positive and negative electrode potentials of the battery. It is important to note that the potential drop across the electrolyte is included in the two half-cell electrode potential readings. This is attributed to the fact that the reference electrode was placed in the middle of the electrolyte layer.

In order to ensure the position of the tungsten reference electrode is in the middle of the electrolyte layer, the battery was charge-discharge cycled within a relatively narrow range of SOC (i.e. between 66.6 % and 76.6 % SOC). In a charge-discharge cycle at 60 mA cm^{-2}, the electrode potential and cell voltage profiles were illustrated in Figure 10. In both processes,

the potential profiles were relatively flat as a small amount of active materials were used in the 1 h charge – 1 h discharge regime. In the charging process, the negative and positive electrode potentials were *c.a.* –0.508 V *vs.* W and +0.029 V *vs.* W, respectively. On the other hand, the potential values in the discharge processes were –0.440 V *vs.* W and –0.050 V *vs.* W, respectively. These potential values gave the overall cell voltages of 0.53 and 0.39 V in the charge and discharge processes, leading to a voltage efficiency of *c.a.* 74 %.

In the charge-discharge processes, the potential profiles of the half-cell electrodes were evaluated at current densities between 20 and 80 mA cm^{-2}. As shown in Figure 11, significant increases in potential drops between the charge and discharge processes were observed at higher current densities. As a result, the voltage efficiencies decreased from 89.9 % at 20 mA cm^{-2} down to 64.9 % at 80 mA cm^{-2}. On the contrary, the duration of the discharge processes remained 1 h after charge-discharge cycled at these current densities.

To evaluate the individual potential drop or polarization of each battery component, the cell voltage in charge and discharge processes can be expressed as:

$$E_{cell\,charge} = E_{pos\,o.c.} - E_{neg\,o.c.} + \sum |\eta| + \sum IR_{electrolyte\,resistance} \tag{8}$$

and

$$E_{cell\,discharge} = E_{pos\,o.c.} - E_{neg\,o.c.} - \sum |\eta| - \sum IR_{electrolyte\,resistance} \tag{9}$$

where $E_{pos\,o.c.}$ and $E_{neg\,o.c.}$ are the open-circuit potentials of the positive and negative half-cell reactions, respectively. The term $IR_{electrolyte\,resistance}$ represents the potential drop across the electrolyte.

This is because the measurements of the half-cell electrode potentials not only take account of the overpotentials but also the ohmic drop across the solution between the electrode of

interest and the reference electrode. The polarization of the half-cell reaction, η, and its corresponding ohmic drop of electrolyte were obtained by subtracting the measured electrode potential value from its open circuit potential. Together with the ohmic drop of the overall battery, these values were measured at different current densities at 700 °C. As shown in Figure 12, the area resistance of the negative electrode, positive electrode (including electrolyte resistances) and the overall cell were 0.55, 0.65 and 1.20 Ω cm^2, respectively.

As reported by Kim *et al.* [15] in their liquid metal batteries, the contribution of the ohmic resistance across the electrolytes in a three electrode set-up was not significant (*c.a.* 0.07 Ω cm^2) at 600 °C. Regarding the geometry of the reference electrode, the ohmic resistance of the battery was determined to be increased by an average of 0.08 Ω cm^2 for each centimetre distance from the negative and positive electrodes in the chloride melt electrolyte. The polarization of the negative and positive electrodes were comparable to those of the calcium-bismuth electrodes (0.5 – 1 Ω cm^2) depending on the equilibrium potentials and the compositions of the alloys.

3.3. Galvanostatic charge-discharge experiment

Figure 13 shows the cell voltage and the half-cell electrode potentials *vs.* time responses of the magnesium-antimony battery under charge-discharge cycling (1 h charge – 1 h discharge regime) at 60 mA cm^{-2} (72 mA) for 8 cycles. The half-cell measurements indicated that the boron nitride layer of the reference electrode was chemically stable and acted as an effective electrical insulator at high temperature (700 °C). In the initial cycles, the voltage and energy efficiencies of the battery were up to 72.8 and 72.2 %, respectively. After subsequent cycles, a slight deterioration in terms of higher charge and lower discharge voltages was observed.

This can be attributed to the inefficient dissolution of the magnesium ions from the antimony alloys and the non-uniform deposition of such alloys in the charge and discharge processes, respectively.

In the cycling test, the coulombic effiency maintained about 99 %, while the voltage efficiencies dropped steadily from *c.a.* 73 % down to *c.a.* 56 % after the 8th cycles. The average energy efficiency of this cycling test was *c.a.* 64 %. The obtained energy efficiencies were comparable to those reported liquid metal batteries in the literatures, including systems based on bismuth and antimony chemistries (> 60 % for higher than 20 mA cm^{-2}) [15, 16]. The energy efficiency of this work is also highly similar to those of the previous magnesium-antimony system of Bradwell *et al.* [12] at similar current densities (*c.a.* 80 % at 18 mA cm^{-2}).

4. Conclusion

In this work, a small-scale liquid metal battery with a simple configuration of reference electrode has been introduced. Within the three floating liquid layers, a tungsten wire was used as the pseudo-reference electrode, which was sprayed by an insulating layer of boron nitride and was immersed in the middle of the electrolyte layer to avoid direct electrical contact with the other electrodes. The incorporation of the reference electrode enables the measurements of the polarizations and half-cell electrode potentials in different battery processes. Experimental results show that the magnesium-antimony battery was capable of charge-discharge cycling at relatively high energy efficiencies (> 60 %) under a range of current densities between 15 and 80 mA cm^{-2}.

In this range, the area resistance of the negative and positive electrodes were *c.a.* 0.55 and 0.65 Ω cm^{-2}, respectively. This suggests that reducing the polarizations of the two electrodes

is necessary to further improve the cell voltage and system efficiencies. Furthermore, the half-cell measurements also indicated that the sprayed layer of boron nitride at the reference electrode was chemically stable and shown to be an effective electrical insulator for prolonged operation at high temperature (700 ^{o}C). Future works should include a movable reference electrode system subjected to the change of SOC to ensure that the position of the reference electrode is in the middle of the electrolyte layer in all charge-discharge processes.

References

1. J. Liu, J.G. Zhang, Z. Yang, J.P. Lemmon, C. Imhoff, G.L. Graff, L. Li, J. Hu, C. Wang, J. Xiao, G. Xia, V.V. Viswanathan, S. Baskaran, V. Sprenkle, X. Li, Y. Shao, B. Schwenzer, Materials science and materials chemistry for large scale electrochemical energy storage: From transportation to electrical grid, *Adv. Funct. Mater.*, 23, 2013, pp. 929 – 946.

2. Z. Yang, J. Zhang, M.C.W. Kintner-Meyer, X. Lu, D. Choi, J.P. Lemmon, J. Liu, Electrochemical energy storage for green grid, *Chem. Rev.*, 111 (2011), pp. 3577-3613.

3. P.K. Leung, Q. Xu, T.S. Zhao, High-potential zinc-lead dioxide rechargeable cells, *Electrochim. Acta*, 79 (2012), -pp. 117-125.

4. P. Leung, X. Li, C. Ponce de Leon, L. Berlouis, C.T. J. Low, F.C. Walsh, Progress in redox flow batteries, remaining challenges and their applications in energy storage, *RSC Adv.*, 2 (2012), pp. 10125 – 10156.

5. M.R. Mohamed, P.K. Leung, M.H. Sulaiman, Performance characterization of a vanadium redox flow battery at different operating parameters under a standardized test-bed system, *Applied Energy*, 137 (2015), pp. 402-412.

6. P.K. Leung, M.R. Mohamed, A.A. Shah, Q. Xu, M.B. Conde-Duran, A mixed acid based vanadium-cerium redox flow battery with a zero-gap serpentine architecture, *J. Power Sources*, 274 (2015), pp. 651 – 658.

7. X. Lu, G. Xia, J.P. Lemmon, Z. Yang, Advanced materials for sodium-beta alumina batteries: Status, challenges and perspectives, *J. Power Sources*, 195 (2010), pp. 2431-2442.

8. G. Li, X. Lu, C.A. Coyle, J. Y. Kim, J.P. Lemmon, V. L. Sprenkle, Z. Yang, Novel ternary molten salt electrolytes for intermediate-temperature sodium/ nickel chloride batteries, *J. Power Sources*, 220 (2012), pp. 193-198.

9. S. Fujiwara, M. Inaba, A. Tasaka, New molten salt systems for high temperatura molten salt batteries: Ternary and quaternary molten systems based on LiF-LiCl, LiF-LiBr, and LiCl-LiBr, *J. Power Sources*, 195 (2010), pp. 7691 – 7700.

10. D. Sadoway, G. Ceder, D. Bradwell, High-amperage energy storage device and method, US Patent application, US 2008/0044725 A1, 2008.

11. K. Wang, K. Jiang, B. Chungm T. Ouchi, P.J. Burke, D.A. Boysen, D.J. Bradwell, H. Kim, U. Muecke, D.R. Sadoway, *Nature*, 514 (2014), pp. 348 – 350.

12. D.J. Bradwell, H. Kim, A.H.C. Sirk, D.R. Sadoway, Magnesium-antimony liquid metal

battery for stationary energy storage, *J. Am. Chem. Soc.*, 134 (2012), pp. 1895-1897.

13. H. Kim, D.A. Boysen, J.M. Newhouse, B.L. Spatocco, B. Chung, P.J. Burke, D.J. Bradwell, K. Jiang, A.A. Tomaszowska, K. Wang, W. Wei, L.A. Ortiz, S.A. Barriga, S.M. Poizeau, D.R. Sadoway, Liquid-metal batteries: Past, present, and future, *Chem. Rev.*, 113 (2013), pp. 2075-2009.

14. H. Kim, D.A. Boysen, D.J. Bradwell, B. Chung, K. Jiang, A.A. Tomaszowska, K. Wang, W. Wei, D.R. Sadoway, Thermodynamic properties of calcium-bismuth alloys determined by emf measurements, *Electrochim. Acta*, 60 (2012), pp. 154-162.

15. H. Kim, D.A. Boysen, T. Ouchi, D.R. Sadoway, Calcium-bismuth electrodes for large-scale energy storage (liquid metal batteries), *J. Power Sources*, 241 (2013), pp. 239 - 248.

16. X. Ning, S. Phadke, B. Chung, H. Yin, P. Burke, D.R. Sadoway, Self-healing Li-Bi liquid metal battery for grid-scale energy storage, *J. Power Sources*, 275 (2015), pp. 370 – 376.

17. F. Stefani, T. Weier, T. Gundrum, G. Gerbeth, How to circumvent the size limitation of liquid metal batteries due to the Tayler instability, *Energy Conversion and Management*, 52 (2011), pp. 2982-2986.

18. M. Seilmayer, F. Stefani, T. Gundrum, T. Weier, G. Gerbeth, M. Gellert, G. Rudiger, Experimental Evidence for a Transient Tayler Instability in a Cylindrical Liquid-Metal Column, *Phys. Rev. Lett.*, 108 (2012), pp. 244501.

19. N. Weber, V. Galindo, F. Stefani, T. Weier, T. Wondrak, Numerical simulation of the Tayler instability in liquid metals, *New J. Phys.*, 15 (2013), 043034.

20. N. Weber, V. Galindo, F. Stefani, T. Weier, Current-driven flow instabilities in large-scale liquid metal batteries, and how to tame them, *J. Power Sources*, 265 (2014), pp. 166 – 173.

21. H. Okamoto, Mg-Sb (Magnesium-Antimony), *JPEDAV*, 31 (2010), 574.

22. A. E. Gheribi, C. Robelin, S. L. Digabel, C. Audet, A.D. Pelton, Calculating all local minima on liquidus surfaces , *J. Chem. Thermodynamics*, 43 (2011), pp. 1323 – 1330.

23. M. Misra, K.S. Raja, J. Ruppert, Electrochemical Corrosion Behavior of Refractory Metals in LiCl-Li$_2$O Molten Salt, ECS Trans, 33 (2010), pp. 181 – 192.

24. J.R. MacDonald, Impedance Spectroscopy – Theory, Experiments and Applications, Wiley, Section 4.52, p.g. 444 – 452.

Figure captions:

Figure 1.   The mechanism of the magnesium-antimony liquid metal battery in the charge-discharge cycling process.

Figure 2.   Magnesium-antimony phase diagrams [21].

Figure 3.   Liquidus projection of the ternary halide salts (KCl, NaCl and $MgCl_2$) system.

Figure 4.   Experimental set-up of the magnesium-antimony liquid metal battery.

Figure 5.   Energy-dispersive X-ray spectroscopy (EDS) of the negative and positive electrodes after cooling down to room temperature.

Figure 6.   Optical and scanning electron micrograph images of the boron nitrite layers before and after immersion of the chloride melts for more than 4 days at 700 ^{o}C.

Figure 7.   The influence of temperature (450 – 780 ^{o}C) on the open-circuit voltage of the magnesium-antimony liquid metal battery.

Figure 8.   Nyquist plots and the equivalent electrical circuit model of the magnesium-antimony liquid metal battery at different temperatures (550, 600, 650 and 700 ^{o}C)

Figure 9.   Linear sweep voltammogram of the magnesium-antimony liquid metal battery by sweeping the cell voltage linearly from – 0.5 to + 1.5 V at a scan rate of 20 mV s^{-1}. Temperature: 700 ^{o}C.

Figure 10.   Electrode potential vs. time behaviours of the magnesium-antimony liquid metal battery under a typical 1 h charge – 1 h discharge cycle at 60 mA cm^{-2}. Temperature: 700 ^{o}C.

Figure 11.   Electrode potential vs. time responses of the magnesium-antimony liquid metal battery under typical 1 h charge – 1 h discharge cycles at current densities ranging from 20 mA cm^{-2} to 80 mA cm^{-2}. Temperature: 700 ^{o}C.

Figure 12.   Effect of current density (10 – 120 mA cm^{-2}) on the half-cell polarizations of the magnesium-antimony liquid metal battery during charge-discharge cycles. Temperature: 700 ^{o}C.

Figure 13.   The half-cell potentials and cell voltage of the magnesium-antimony liquid metal battery during an experiment using a 1 h charge-1 h discharge regime at 60 mA cm^{-2} for the first 8 cycles.
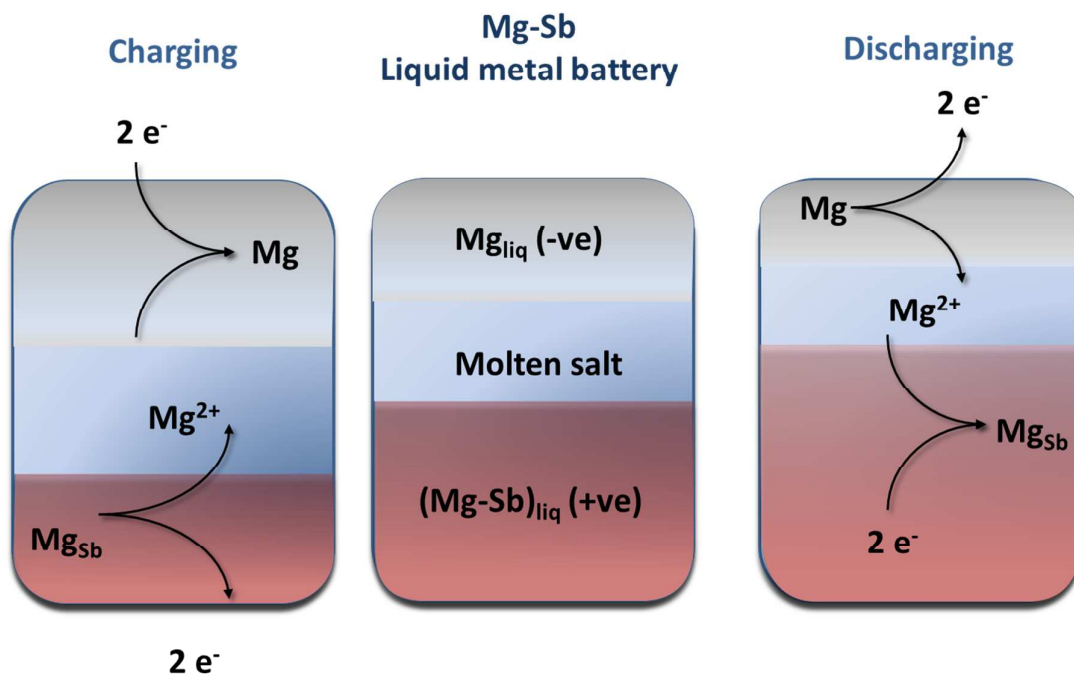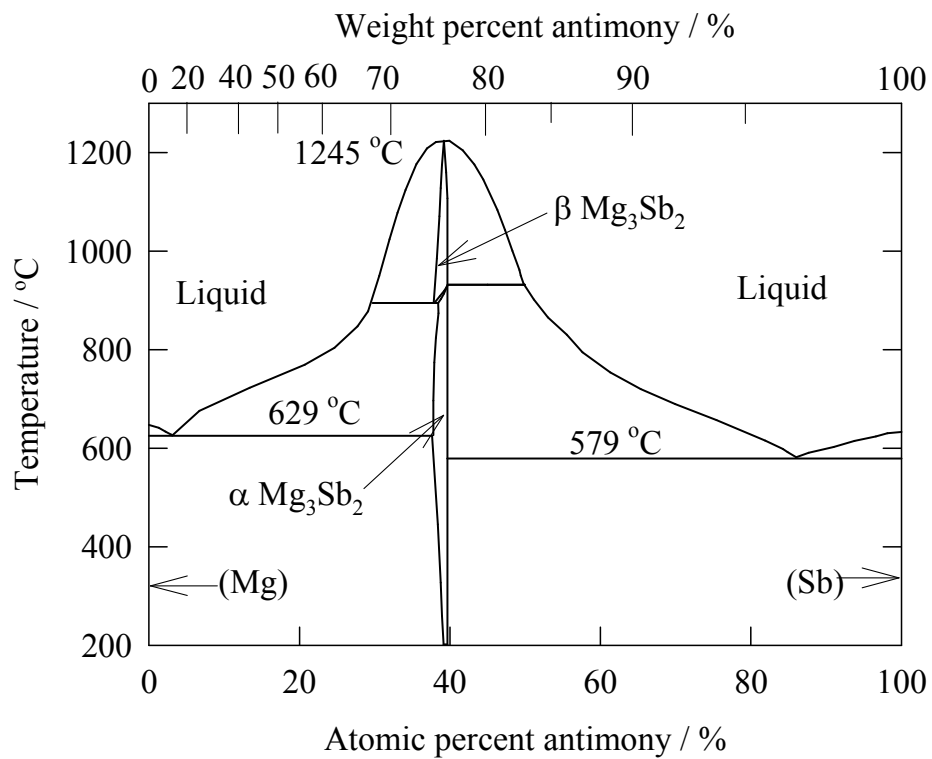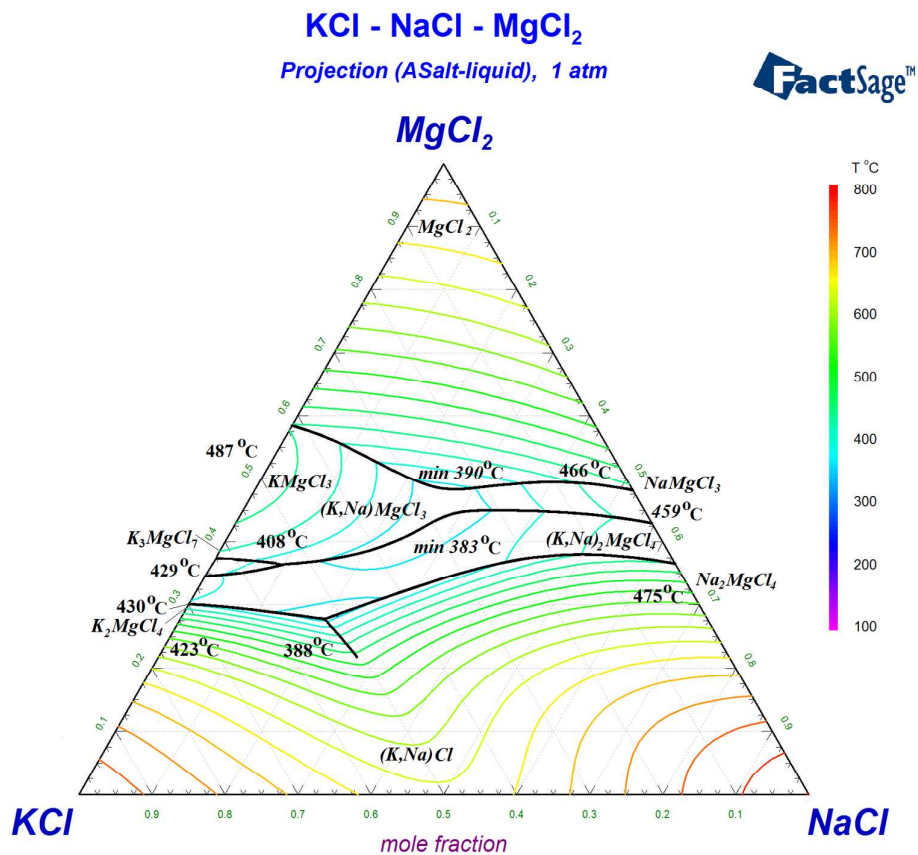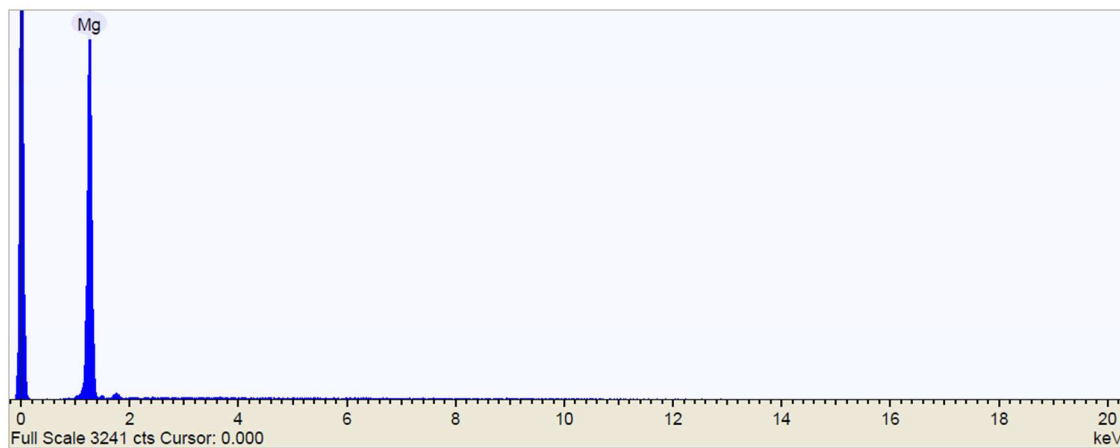
1

Figure 1

Figure 2
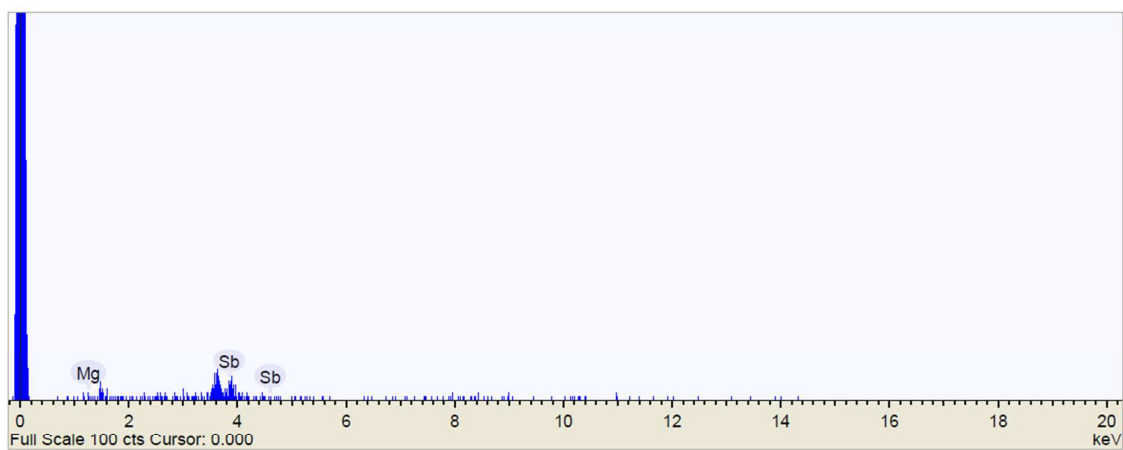
Figure 3

4

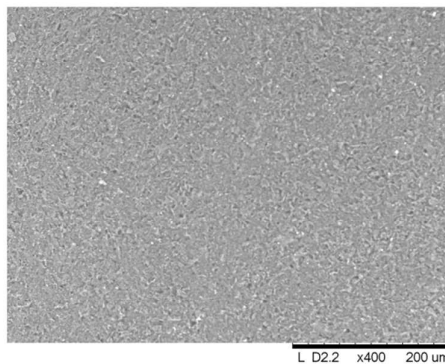**Magnesium negative electrode**

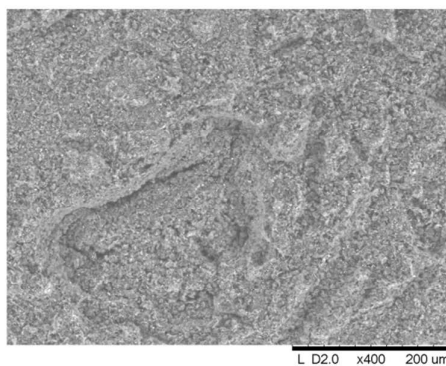**Antimony positive electrode**

Figure 4

5

Optical images   **Scanning Electron Micrograph images**

L D2.2   x400   200 um

Before immersion in chloride melt
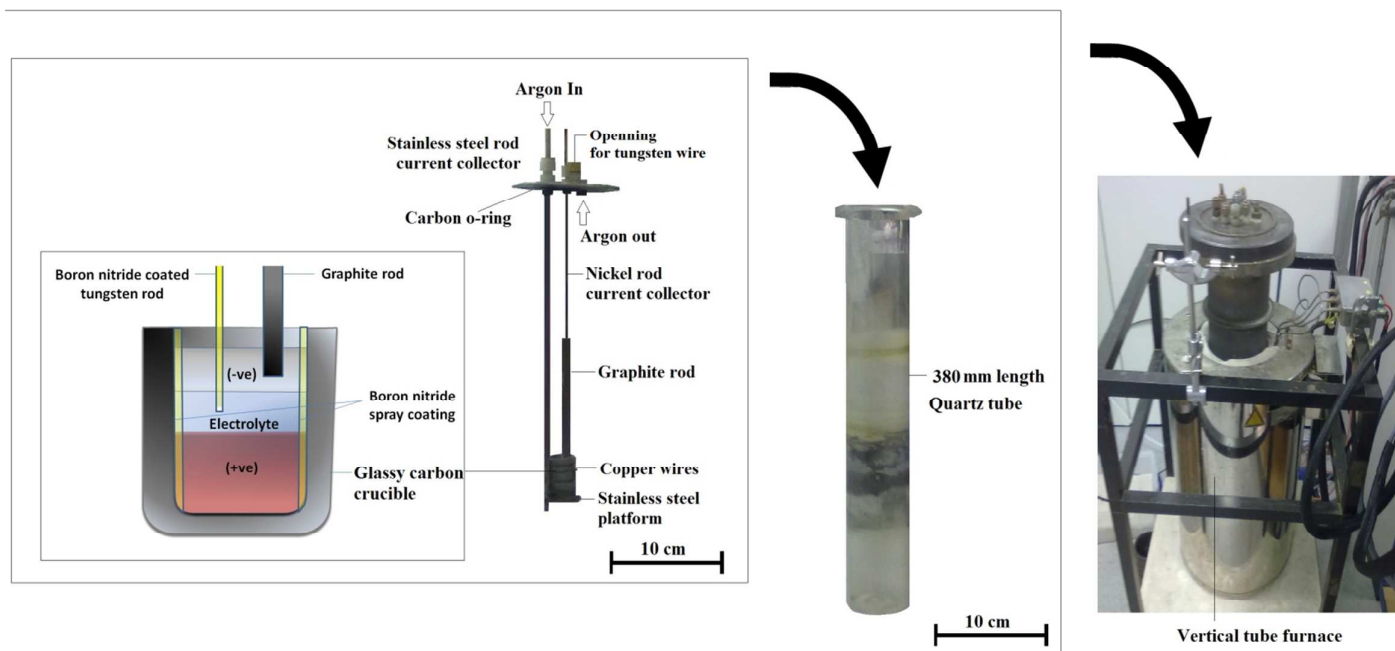

L D2.0   x400   200 um
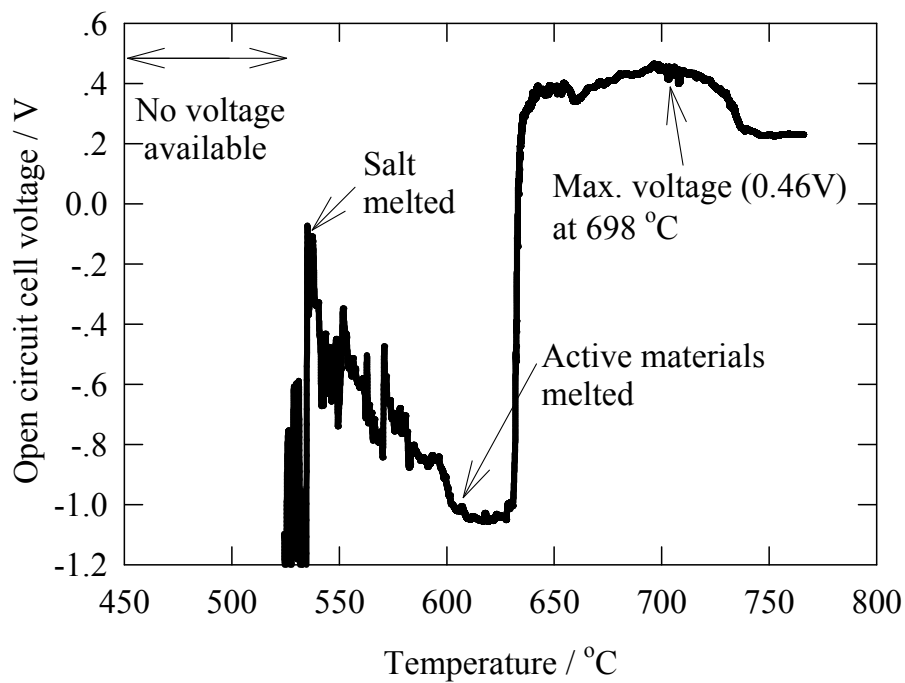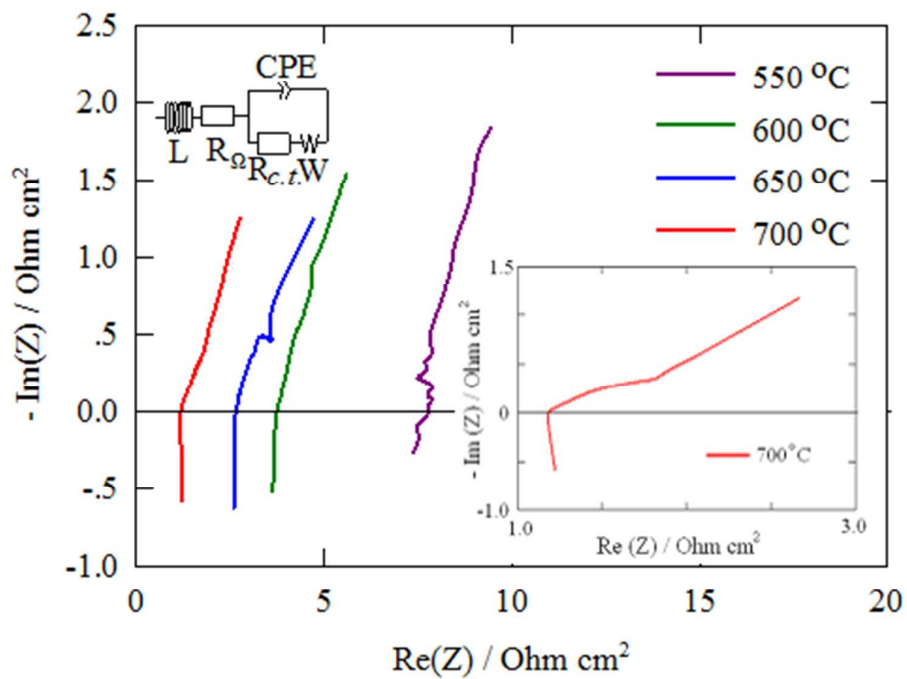
After immersion in chloride melt
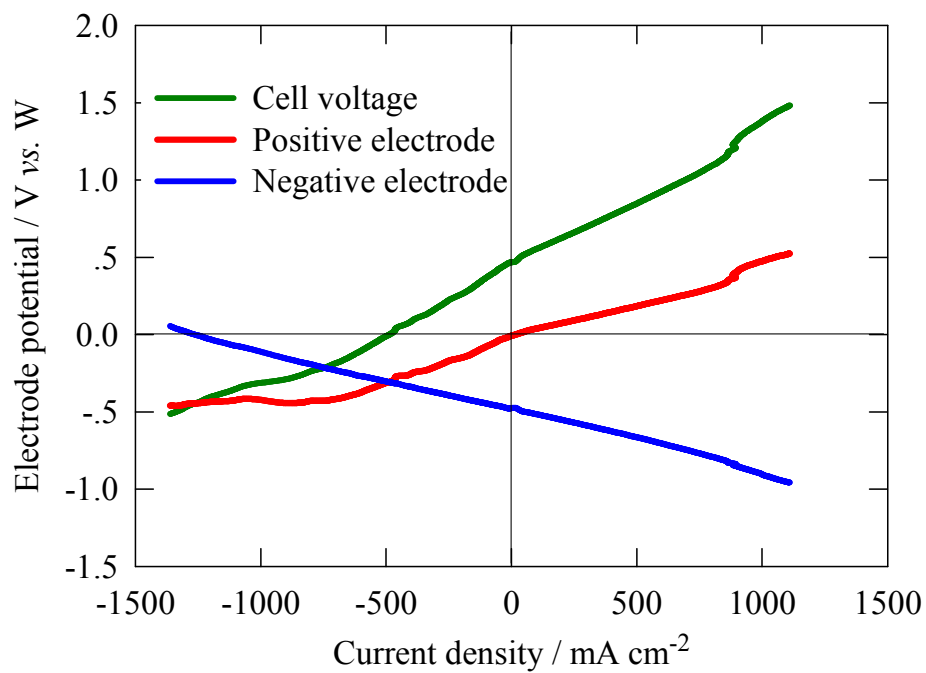
Figure 5

6

Figure 6

Figure 7

7

Figure 8

Figure 9

8
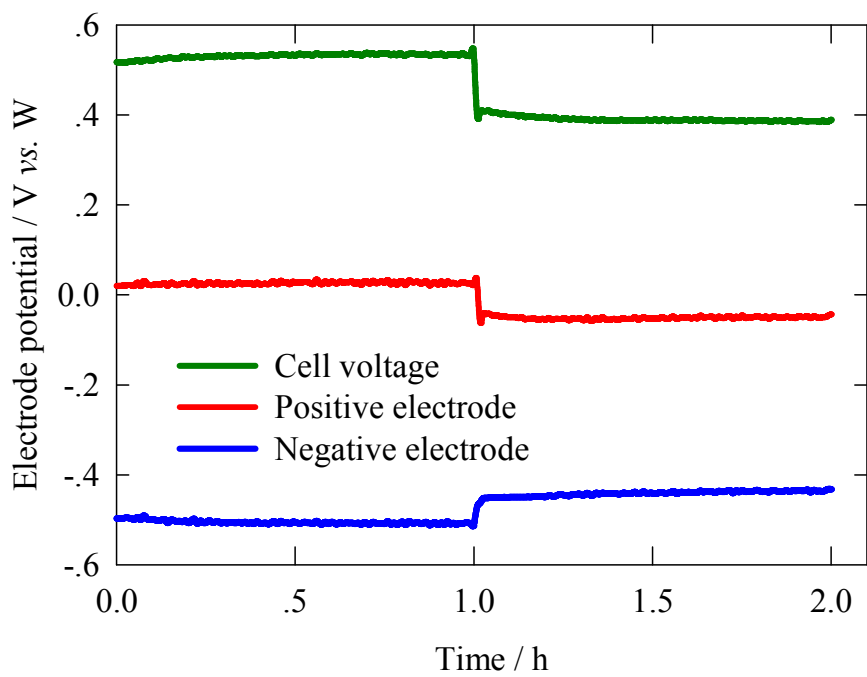
Figure 10

Figure 11

9
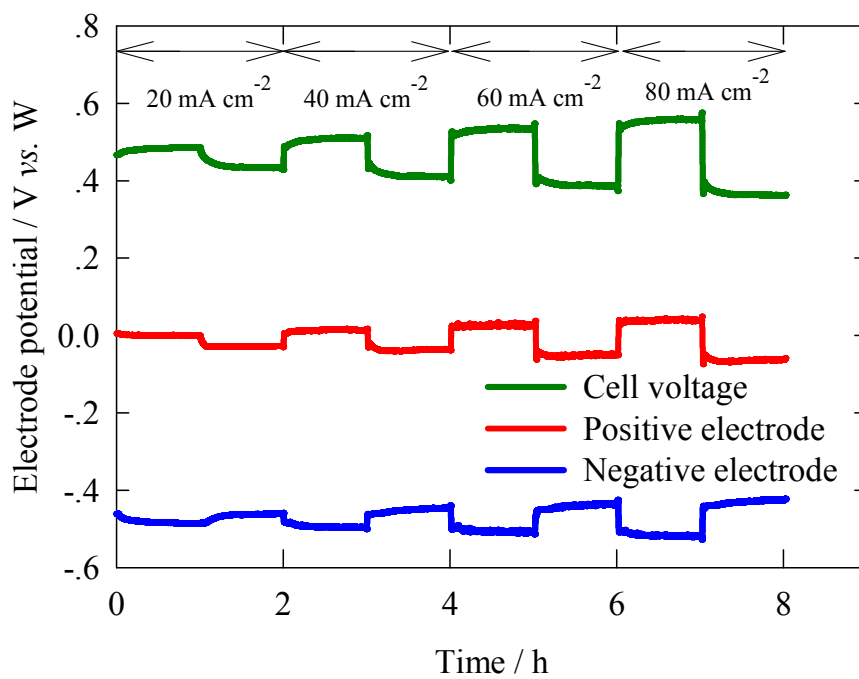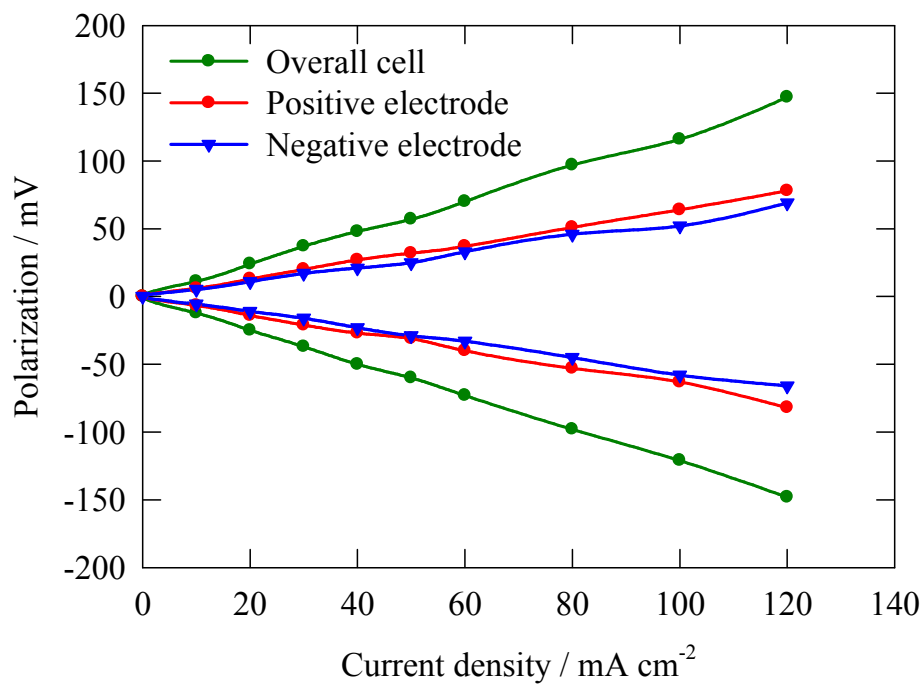
Figure 12

Figure 13

10

11

1
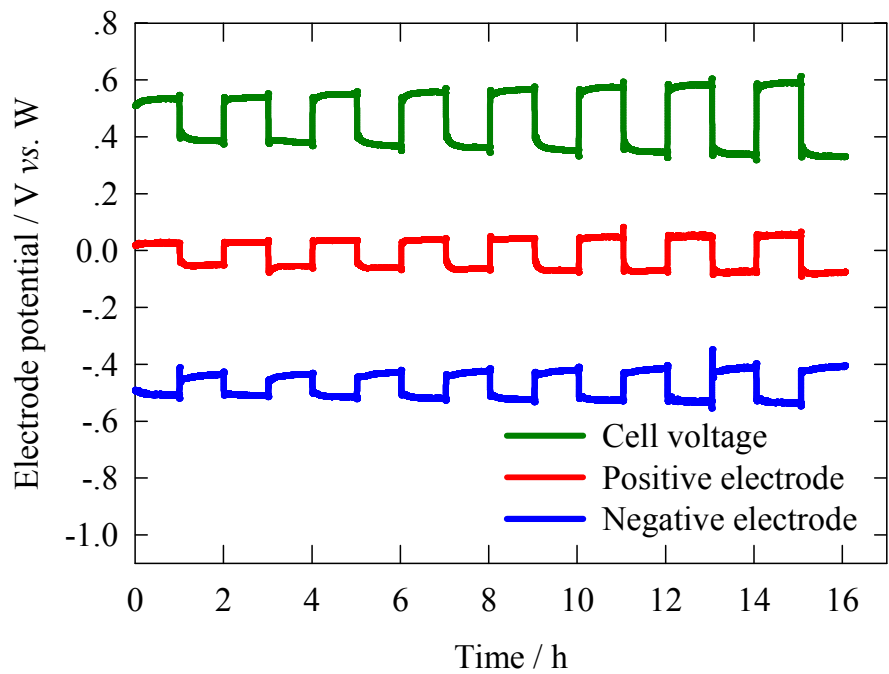
Temperature /^{o}C	550	600	650	700
L / H	3.76×10^{-7}	3.06×10^{-7}	3.70×10^{-7}	3.37×10^{-7}
R_Ω / Ohm cm^2	7.48	3.66	2.63	1.20
Q / F s$^{(a-1)}$	0.22	0.22	0.16	0.26
a	0.60	0.53	0.56	0.8
$R_{c.t.}$ / Ohm cm^2	10.53	5.40	1.50	0.39
σ	4.2	2.23	0.95	0.27

2   Table 1. Equivalent circuit model fit results to the electrochemical impedance spectra.

Charging

**Mg-Sb
Liquid metal battery**

Discharging

2 e⁻

Mg

Mg_{liq} (-ve)

Mg

2 e⁻

Mg^{2+}

Molten salt

Mg^{2+}

Mg_{Sb}

$(Mg-Sb)_{liq}$ (+ve)

Mg_{Sb}

2 e⁻

2 e⁻